

## Article

# A Study and Implementation of Inductive Power Transfer System Using Hybrid Control Strategy for CC-CV Battery Charging

Liangxi He <sup>1</sup>, Xiaoqiang Wang <sup>2</sup> and Chi-Kwan Lee <sup>1,\*</sup><sup>1</sup> Department of Electrical and Electronic Engineering, The University of Hong Kong, Hong Kong 999077, China<sup>2</sup> College of Electrical Engineering, Zhejiang University, Hangzhou 310058, China

\* Correspondence: ckleee@eee.hku.hk

**Abstract:** In this paper, a hybrid control strategy is studied and implemented on an Inductive Power Transfer (IPT) system to simultaneously realize zero-voltage switching (ZVS) and constant current (CC) and constant voltage (CV) battery charging. A steady-state analysis of pulse frequency modulation was conducted, based on the characteristic of voltage gain versus switching frequency, and CC and CV charging modes were promised. The ZVS of the inverter was obtained by satisfying the minimum requirement of full discharge of the junction capacitor on the MOSFETs using a commutation current during the dead-time interval. Two control degrees of freedom are needed to realize the two control targets. This hybrid control strategy adopts a self-oscillating (SO) control to achieve ZVS and phase shift (PS) control and a constant output for the series-series (SS)-compensated IPT system. To validate the hybrid control strategy, a 1.6 kW prototype with 360–440 V input voltage and 250–400 V output voltage was built and the experimental results show that the peak efficiency can reach 96.1%. Compared with the conventional variable frequency (VF) control, the hybrid control method proves that an additional control variable can fulfill the control target in a more flexible manner, which makes the switching frequency close to the resonant frequency during the charging process, minimizing the reactive current in the resonant tank and improving system efficiency.

**Keywords:** constant current/voltage (CC/CV); hybrid control; inductive power transfer; optimal ZVS tracking; self-oscillation



**Citation:** He, L.; Wang, X.; Lee, C.-K. A Study and Implementation of Inductive Power Transfer System Using Hybrid Control Strategy for CC-CV Battery Charging. *Sustainability* **2023**, *15*, 3606. <https://doi.org/10.3390/su15043606>

Academic Editor: J. C. Hernandez

Received: 16 January 2023

Revised: 6 February 2023

Accepted: 10 February 2023

Published: 15 February 2023



**Copyright:** © 2023 by the authors. Licensee MDPI, Basel, Switzerland. This article is an open access article distributed under the terms and conditions of the Creative Commons Attribution (CC BY) license (<https://creativecommons.org/licenses/by/4.0/>).

## 1. Introduction

Inductive power transfer (IPT) has attracted attention in recent years because of its high reliability, safety, and convenience. It has been utilized in numerous applications, such as medical implantable pacemakers, portable electronic devices, electric vehicles (EVs), and railway transportation. EVs not only consume renewable energy but also act as a movable power supply. IPT facilitates convenient interactions between EVs and power grids. The IPT technology used for battery charging in EVs is one of the most promising applications, and the employment of IPT will considerably alleviate range anxiety. Therefore, the IPT battery-charging technique is of great importance in the development of the EVs in the future [1–14].

In order to prevent degradation of battery life and improve the efficiency of the charging system, some key issues remain to be addressed. For practical applications, a constant current (CC) and constant voltage (CV) are always essential in the charging profile, as the equivalent resistance of battery varies dynamically during the charging process [7]. Besides, it is crucial to minimize the reactive current within the charging process on the premise of a zero-voltage switching (ZVS) operation [15,16], where ZVS can lead to reduced switching loss and eliminate some of the sources of converter-generated electro-magnetic interference (EMI) [17].

According to a literature review, the variable compensation topology has been widely utilized in battery-charging systems [18–20] and its basic principle involves changing the resonant tank by using additional switches to implement a CC- and CV-mode charge operation. As a result, the IPT battery-charging system can achieve a zero phase angle (ZPA) operation and thereby reduce the reactive current. The adoption of additional switches should be circumvented to the utmost as it may degrade the system efficiency. In [21,22], double-sided LCC-compensated IPT charging systems are presented to realize load-independent CC and CV outputs at two different switching frequencies.

The control strategy is an acceptable alternative to fulfill the charging profile using simple compensation topologies. They can be roughly categorized as pulse width modulation (PWM), pulse density modulation (PDM), phase shift (PS), variable frequency (VF), and self-oscillation (SO), etc. [23–27]. In [23], PS control is adopted to realize a constant current or voltage output, but it has a serious deficiency: ZVS cannot be achieved throughout the whole charging process. In [24], VF control is employed to regulate the output voltage with ZVS for a series–series (SS)-compensated IPT system. Aside from the high reactive current and component stresses caused by the switching frequency's deviation from the resonant frequency, frequency bifurcation may occur when multiple frequencies can satisfy ZVS operation, resulting in system instability. In [25], a PDM ZVS full bridge converter for an IPT system is proposed to eliminate the dependence on coupling and load conditions, but this needs an LC branch to provide the ZVS current, resulting in additional power losses. In [26,27], SO control is presented for an SS-compensated IPT converter. They mainly focus on the frequency tuning and dynamic response instead of the regulation of output power.

At least two control degrees of freedom are needed to simultaneously realize the two control targets, i.e., the constant output and ZVS. Therefore, the other potential solutions to the above-mentioned issues fall on hybrid control strategies. In [28], the combination of PWM and phase-locked loop (PLL) is proposed to realize a constant output voltage and ZVS operation. A new SO-tuning loop for IPT systems with PS and PWM control is proposed, while the characteristics of battery charging are not investigated [29]. In [30,31], VF and PS hybrid control strategies are presented for battery-charging systems. Hybrid control may suffer from hard switching, especially under light load conditions [32]. In [33], a coordination control of PS and an auxiliary variable inductor (VI) installed in the primary side are proposed to achieve stable output and extend the ZVS operation range. In [34], a dynamic tuning method of ZVS angle using a variable capacitor is proposed, and PS is implemented to achieve a constant output. In [35], it is proven that hybrid controllers can serve a lot better than standalone controllers in precise control applications.

A hybrid control strategy for CC-CV battery charging and ZVS tracking is studied and implemented in this paper. The main contributions of this paper are summarized as follows.

The analysis of a series–series (SS)-compensated IPT system is conducted, looking at the control target, steady-state analysis of pulse frequency modulation, ZVS tracking, and limits on the degree of freedom for VF control. During implementation, using the characteristics of the voltage gains versus switching frequency, the CC- and CV-charging modes can be achieved. Meanwhile, ZVS tracking is analyzed in detail. This reveals that the minimum requirement to realize ZVS is to discharge the junction capacitor on the MOSFETs, which is highly related to the drain-source voltage, dead-time interval, and commutation current. Two types of control strategies, i.e., VF and SO-PS, are discussed. This shows that the VF control strategy will be further from the natural resonant frequency, while the adoption of an additional control variable phase shift helps to complete the same control target in a more flexible way.

The rest of the paper is organized as follows. Section 2 details the steady-state characteristic of the SS-compensated IPT system. In Section 3, the implementation of a hybrid control strategy is presented. In Section 4, an experimental prototype with 360–440 V input voltage and 250–400 V output voltage is built to verify the hybrid control strategy. Finally, the conclusion is given in Section 5.

## 2. Analysis of SS-Compensated IPT System

Figure 1 shows the circuit architecture of the SS-compensated IPT charging system. The high-frequency inverter has a full bridge consisting of four power MOSFETs ( $S_1$ – $S_4$ ).  $V_{in}$  and  $v_p$  denote the DC and AC voltages of the inverter, respectively. The rectifier comprises four diodes ( $D_1$ – $D_4$ ) and a filter capacitor  $C_o$ .  $v_s$  is the output voltage before the rectifier.  $V_o$  and  $I_o$  are the output voltage and current of the IPT charging system.  $L_p$  and  $L_s$  are the self-inductance of the primary and secondary coils.  $M$  is the mutual inductance between two coils, and the coupling coefficient is  $k = M/(L_p L_s)^{1/2}$ .  $C_p$  and  $C_s$  are resonant capacitors that are used to compensate  $L_p$  and  $L_s$ .

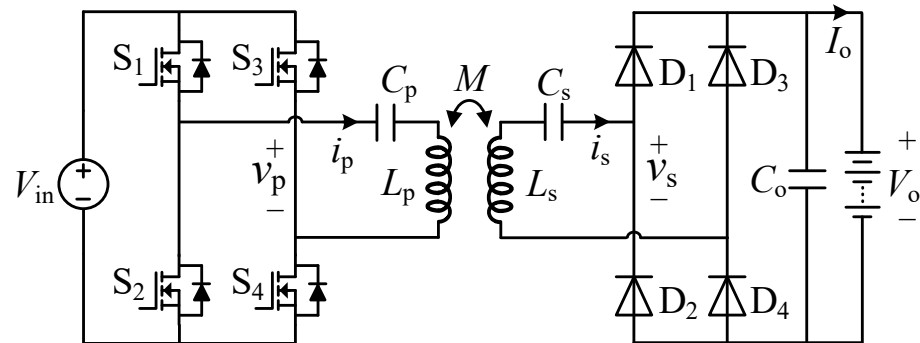


Figure 1. Circuit architecture of SS-compensated IPT charging system.

For simplicity, the resonant frequency between the primary side and secondary side are set to be equal, which satisfies:

$$\omega_r = \frac{1}{\sqrt{L_p C_p}} = \frac{1}{\sqrt{L_s C_s}} \quad (1)$$

The transferred power of the IPT system is mainly related to the fundamental component while the high-order harmonics contribute little to the power transfer. To simplify the analysis, the fundamental harmonic approximation (FHA) is used. The ac equivalent circuit model is shown in Figure 2.  $\omega$  denotes the switching angular frequency.

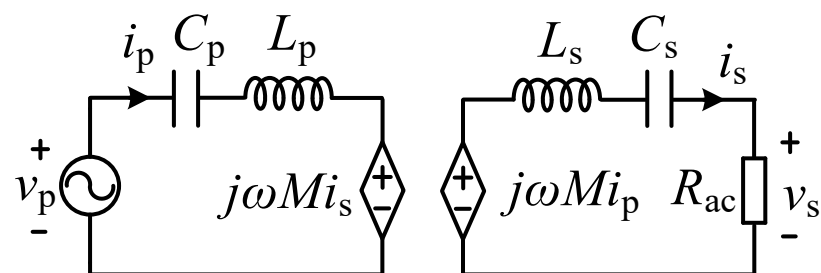


Figure 2. The ac equivalent circuit of the SS-compensated IPT system.

The fundamental component of  $v_p$  is derived as:

$$v_p = \frac{2\sqrt{2}}{\pi} V_{in} \quad (2)$$

According to Kirchhoff's law, the ac equivalent circuit can be expressed by:

$$\begin{cases} v_p = j\left(\omega L_p - \frac{1}{\omega C_p}\right) i_p - j\omega M i_s \\ v_s = j\omega M i_p - j\left(\omega L_s - \frac{1}{\omega C_s}\right) i_s \end{cases} \quad (3)$$

### 2.1. System Specifications

In general, Li-ion battery cells are commonly used for high-voltage battery packs. As indicated, the cell voltage exhibits a wide voltage range (1–4.2 V) throughout the whole charging process. In this paper, the voltage range of the battery pack is 250–400 V. The maximum charging current of the battery pack is 4 A. Figure 3 illustrates a simplified battery charging profile. There are two sequential processes: CC mode and CV mode.

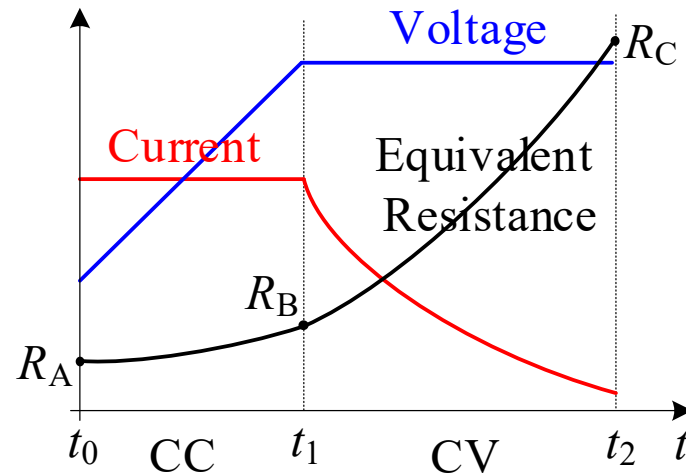


**Figure 3.** The simplified battery charging profile.

From Figure 3, the battery pack appears to the IPT charger as a variable equivalent resistance  $R_L$ , which is defined as the ratio of charging voltage to current. During the CC mode (between the time interval  $t_0$  and  $t_1$ ), the corresponding equivalent resistance of the battery packs increased from  $R_A$  (62.5  $\Omega$ ) to  $R_B$  (100  $\Omega$ ). In the CV mode, the charging current will decrease, and the maximum equivalent resistance is  $R_C$  (800  $\Omega$ ).

It should be noted that the nominal input voltage of the IPT charger from the front-end AC/DC converter varies between 360 V and 440 V (400 V  $\pm$  10%). Table 1 shows the electrical specification of the IPT charging system.

**Table 1.** Electrical specifications.

Parameters	Symbol	Value
Input voltage $V_{in}$	$V_{in\_min} - V_{in\_max}$	360–440 V
Output voltage $V_{out}$	$V_{out\_min} - V_{out\_max}$	250–400 V
Maximum output power	$P_{o\_max}$	1.6 kW
Air gap	$d$	10–15 cm
Maximum coil diameter	$D_{out}$	30 cm
Load resistance	$R_L$	62.5–800 $\Omega$

### 2.2. Steady-State Analysis of Pulse Frequency Modulation

Normalized parameters help to find the transfer function of the IPT system. These equations are defined and explained as follows:

$$\alpha = \frac{L_p}{L_s} \quad \gamma = \frac{\omega}{\omega_r} \quad X_{Ls} = \omega_r L_s \quad Q = \frac{\pi^2 X_{Ls}}{8R_L} \quad (4)$$

where  $\alpha$  is the inductance ratio of transmitter coil over receiver coil,  $\gamma$  is the normalized switching frequency in terms of primary natural resonant frequency  $\omega_r = 1/\sqrt{L_p C_p}$ ,  $X_{Ls}$  stands for the impedance of  $L_s$  and  $Q$  stands for the load quality factor.

From (3), the current of transmitter coil can be derived as

$$i_p = \left| \frac{v_p}{\alpha X_{Ls}} \frac{j\gamma(\gamma^2 - 1)Q + \gamma^2}{\gamma^4 k^2 Q - (\gamma^2 - 1)^2 Q + j\gamma(\gamma^2 - 1)} \right| \quad (5)$$

Hence, the steady-state voltage gain  $G_v$  can be expressed as

$$G_v = \left| \frac{j\gamma^3 k \sqrt{\alpha}}{\gamma^4 k^2 \alpha Q - (\gamma^2 - 1)^2 \alpha Q + j\gamma(\gamma^2 - 1)\alpha} \right| \quad (6)$$

According to Figure 2, the input impedance angle  $\varphi$  can be calculated as

$$\varphi = \arctan \frac{\gamma(\gamma^2 - 1)\frac{1}{Q} + (\gamma^2 - 1)^2 Q - \gamma^3 k^2 (\gamma^2 - 1) Q}{\gamma^4 k^2} \quad (7)$$

It is well-known that an SS-compensation topology can achieve both CC output and CV output. To achieve the CC output, the system should be operated at the natural resonance frequency, and the following equation should be satisfied according to Equation (6).

$$\gamma(\gamma^2 - 1)\alpha = 0 \Rightarrow \gamma = 1 \quad (8)$$

When Equation (8) is satisfied, the voltage gain  $G_v$  is inversely proportional to the load quality factor, which means that only CC output is achieved. However, the following stage CV output is hard to realize because the system does not have a good voltage regulation ability unless an additional converter is adopted [36]. Considering the specification listed in Table 1, there are some constraints when the SS-compensated IPT converter operates at the CC output condition, i.e.,  $\gamma = 1$ . Several preliminary limitations can be drawn as follows:

- (1) The inductance of the primary and secondary coil must be quite large to achieve the desired mutual inductance  $M$ . For instance, the output current at  $\gamma = 1$  is approximately inversely proportional to  $M$ , i.e.,  $I_o = V_{in}/(\omega M)$ . Assuming that the operating frequency is 85 kHz and  $k = 0.2$ ,  $M = 187 \mu\text{H}$  and the inductance of  $L_p$  and  $L_s$  is about 0.94 mH. Accordingly, the ac resistance of Litz-wire is quite large, which significantly degrades the overall efficiency.
- (2) The current of primary coil  $i_p$  turns out to be infinite in the absence of a secondary coil, which may damage the switches.

Similarly, the value of  $G_v$  should have no relationship with the load resistance to achieve the CV output, i.e.,

$$\gamma^4 k^2 \alpha - (\gamma^2 - 1)^2 \alpha = 0 \Rightarrow \gamma = \frac{1}{\sqrt{1+k}} \text{ or } \gamma = \frac{1}{\sqrt{1-k}} \quad (9)$$

According to (6) and (7), the voltage gain  $G_v$  and input impedance angle  $\varphi$  versus the normalized switching frequency under different load resistances  $R_L$  are depicted in Figure 4. As previously stated, the desired output voltage gain window is  $[G_{v,\min} G_{v,\max}]$ , where  $G_{v,\min} = V_{o,\min}/V_{in,\max} = 0.562$ ,  $G_{v,\max} = V_{o,\max}/V_{in,\min} = 1.111$ . The voltage controllability is notably enhanced, and both CC and CV output can be realized within this range. For CC output, the  $G_v$  value can be controlled to follow the curve of equivalent resistance  $R_L$  and keep their ratio constant during the charging process, so that CC output can be achieved. For CV output,  $G_v$  remains still.

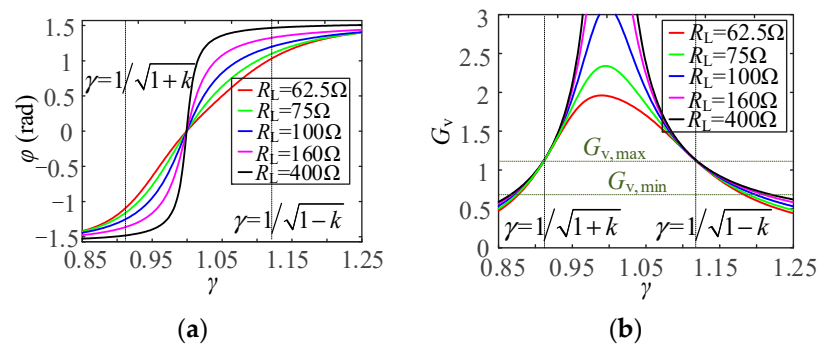


**Figure 4.** The curve of (a)  $\varphi$  (b)  $G_v$  versus different load resistance  $R_L$ .

As seen from Figure 4b, when  $\gamma = 1/\sqrt{1+k}$ , the input impedance is capacitive and the MOSFETs cannot achieve ZVS. However, the input impedance is inductive with when  $\gamma = 1/\sqrt{1-k}$ , which contributes to ZVS operation.

### 2.3. Operation Principle of ZVS Tracking

In order to realize ZVS, the primary coil current  $i_p$  must be large enough to fully discharge the junction capacitors within the dead time before conducting the antiparallel diode. The required charge for a single MOSFET can be represented by the following expression:

$$Q_r = \int_0^{V_{in}} C_{oss}(V_{ds})dV_{ds} \quad (10)$$

where  $C_{oss}$  is the output capacitance and  $V_{ds}$  is the drain-source voltage. It is difficult to directly calculate the output capacitance because  $C_{oss}$  is a nonlinear function of  $V_{ds}$ . However, according to the input voltage range listed in Table 1, it is justifiable to assume that the required charge  $Q_r$  is constant with the MOSFETs datasheet given by manufactures.

Since the dead-time is short enough compared with the switching period, the switching current can be regarded as constant during the ZVS commutation time interval. Consequently, the average commutation current during the dead-time interval can be derived as:

$$|I_{ZVS}| \geq \frac{4C_{oss}V_{in, \max}}{t_d} \quad (11)$$

where  $t_d$  is the dead-time [37].

According to (11),  $I_{ZVS}$  is expected to be larger than the right side of (11) for the realization of ZVS. However, a larger  $I_{ZVS}$  means that more energy is fed back to the input supply by the resonant tank, posing a great challenge to the circuit components due to the high current and voltage stresses. Therefore, a minimized  $I_{ZVS}$  is the best choice for ZVS within the whole load range. In other words, when  $I_{ZVS}$  equals the right side of (11), despite the variation in the coupling coefficient and load resistance, the minimum requirement of ZVS would be satisfied. The minimum average commutation current during the dead-time interval should be the reference value used to design the control loop.

### 2.4. Limitation in Degree of Freedom for VF Control

To adapt to the wide range of output voltage and load resistance, the switching frequency must swing in a wide range for VF control. The typical operating waveforms of VF control are depicted in Figure 5.

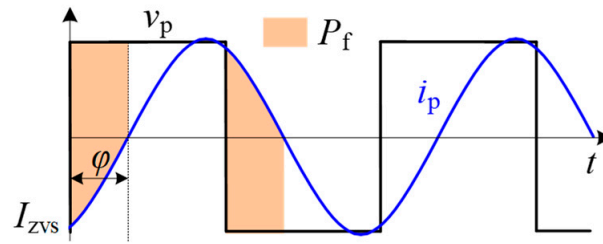


**Figure 5.** The typical operation waveforms of VF control.

Assuming  $i_p(t) = I_p \sin(\omega t - \varphi)$ , the power that is fed back to the input voltage in one cycle period,  $T$ , can be expressed as

$$P_f = \frac{V_{in}}{T} \left[ \int_0^{\frac{\varphi}{\omega}} i_p(t) dt + \int_{\frac{\pi}{\omega}}^{\frac{(\pi+\varphi)}{\omega}} i_p(t) dt \right] \quad (12)$$

where  $I_p$  is the rms value of  $i_p$ .  $P_f$  is represented by a light salmon color in the figure.

Similarly, the power transferred to the secondary side without considering the coil loss, can be written as

$$P_t = \frac{V_{in}}{T} \left[ \int_{\frac{\varphi}{\omega}}^{\frac{\pi}{\omega}} i_p(t) dt + \int_{\frac{(\pi+\varphi)}{\omega}}^{\frac{2\pi}{\omega}} i_p(t) dt \right] \quad (13)$$

At  $t = 0$ ,  $I_{ZVS}$  can be obtained

$$I_{ZVS} = I_p \sin \varphi \quad (14)$$

By combining and solving (12)–(14), it is easy to obtain

$$P_f = P_t \tan^2 \frac{\varphi}{2} \quad (15)$$

$$I_{ZVS} = \frac{P_t}{V_{in}} \tan \frac{\varphi}{2} \quad (16)$$

Figure 4a shows that when the switching frequency deviates from the natural resonant frequency ( $\gamma = 1$ ), the input impedance angle  $\varphi$  increases dramatically. According to (15) and (16), when the power transferred from the primary side to secondary side  $P_t$  is constant, both  $P_f$  and  $I_{ZVS}$  increase with the increase in  $\varphi$ , resulting in higher reactive power losses.

As indicated before, there are two main objectives (CC-CV charging and ZVS) that should be achieved simultaneously to significantly improve the performance of the IPT system. Apparently, the degree of freedom for VF control cannot satisfy the above two objectives concurrently. Thus, an extra control variable should be introduced to increase the degree of freedom of control.

### 3. Implementation of Hybrid Control Strategy

To make the switching frequency close to the natural resonant frequency within the entire load range, in addition to the VF control, an extra PS control is used to regulate the output voltage/current. The key operation waveforms of the VF-PS control are plotted in Figure 6.  $G_1$ – $G_4$  represent the gate signals of power MOSFETs  $S_1$ – $S_4$ , respectively, and  $v_{p,1}$  is the fundamental waveform of  $v_p$ . The phase-shift angle  $\theta$  is defined as the phase difference between the gate signals of switch pairs  $S_2$  and  $S_4$ . It is worth noting that  $\theta$  only affects the rms value of  $v_{p,1}$ , which can be calculated as

$$v_{p,1} = \frac{2\sqrt{2}}{\pi} V_{in} \sin \frac{\theta}{2} \quad (17)$$

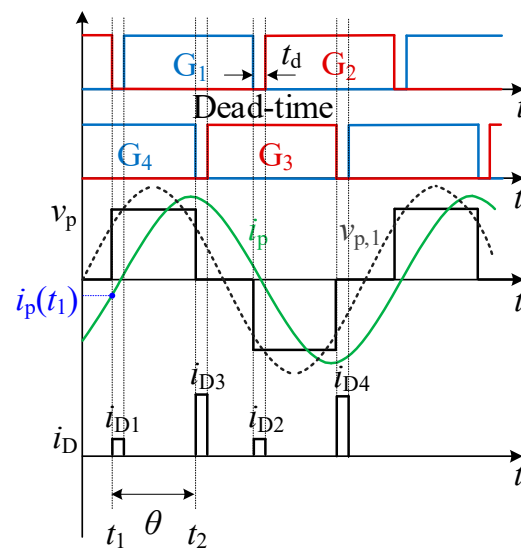


Figure 6. The typical operating waveforms of VF-PS control.

Figure 6 illustrates that, at time  $t_1$ , the gate signal  $G_2$  becomes zero. As the primary-side current  $i_p$  is constant during the dead time interval, the junction capacitor on  $S_1$  starts to discharge, with a commutation current represented by  $i_{D1}$ . The commutation current  $i_{D1}$  discharges the charge  $Q_r$  during the dead time, preparing for the zero-voltage switch-on of  $S_1$ .  $i_{D1}$  equals  $i_{D2}$ , and  $i_{D3}$  equals  $i_{D4}$ . In addition, it is obvious that  $i_{D3}$  is larger than  $i_{D1}$ , which indicates that, if  $S_1$  can realize ZVS, all switches  $S_1$ – $S_4$  can realize ZVS.

From (6) and (17), the steady-state voltage gain  $G$  of VF-PS control can be rewritten as

$$G = \left| \frac{j\gamma^3 k \sqrt{\alpha} \sin \frac{\theta}{2}}{\gamma^4 k^2 \alpha Q - (\gamma^2 - 1)^2 \alpha Q + j\gamma(\gamma^2 - 1)\alpha} \right| \quad (18)$$

According to (18), the 3D gain surfaces  $G$  against  $\gamma$  and  $\theta$  under different loads are depicted in Figure 7. The red and blue curves are the contours of  $G_{\max}$  and  $G_{\min}$ . This shows that, with a constant  $\gamma$ ,  $G$  will decrease as  $\theta$  decreases. When  $\theta$  is fixed,  $G$  shows a single-peak curve, as  $\gamma$  varies if the bifurcation phenomena do not exist [38]. Fortunately,  $G$  is a monotone decreasing function in the inductive region, i.e.,  $\gamma > 1$ , which is crucial to ZVS operation. Theoretically, numerous combinations of  $\gamma$  and  $\theta$  can fulfil the charging profile. However, only one possible combination can fulfil the charging profile. From Figure 7a to c, the load resistance ranges from 62.5  $\Omega$  to 800  $\Omega$ , which demonstrates that the analysis is valid throughout the whole charging process.

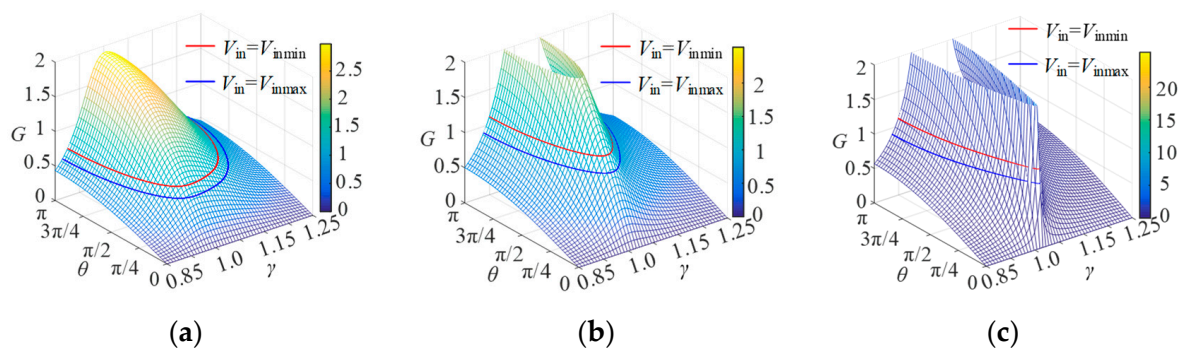


Figure 7. The 3-D gain surfaces  $G$  against  $\gamma$  and  $\theta$  under different loads. (a)  $V_o = 250$  V,  $I_o = 4$  A. (b)  $V_o = 400$  V,  $I_o = 4$  A. (c)  $V_o = 400$  V,  $I_o = 0.5$  A.

### Self-Oscillating Phase Shift Control Strategy

On the basis of preceding analysis, there are two possible implementation schemes for VF-PS control strategy, which can be classified into the following types:

Type-I: The VF control loop is in charge of CC-CV charging while the PS control loop focuses on ZVS.

Type-II: The PS control loop is in charge of CC-CV charging while the VF control loop focuses on ZVS.

In this work, type-II is adopted.

Inspired by [36], the self-oscillating (SO) control strategy is employed to handle the ZVS operation. Unlike the traditional VF control, which externally imposes the switching frequency, SO control can always maintain  $i_p$  lagging after the rising edge of  $v_p$ . The stability of SO can be investigated using the extended Nyquist stability criterion [39,40] and is not discussed here. SO control also tunes the operating frequency. Therefore, SO-PS control is a kind of VF-PS control. Figure 8 illustrates the proposed SO-PS hybrid control diagram of the SS-compensated IPT charging system, where the grey region is analog circuit and light salmon region is MCU. It is known that the detection of a switching current  $i_p(t_1)$ , used to obtain its instantaneous value at  $t_1$ , is unnecessary, since it is easily disturbed by the circuit noise. In this implementation, the current  $i_p$  is sampled by current sensing circuits and filtered through the bandpass filter. To compensate for the phase delay caused by the measurement circuits, a phase-delay compensation circuit is utilized, and its output signal is represented by  $v_{ct}$ . Triggered by  $v_{ct}$ , the hysteresis comparator will produce the driving signal  $S_a$  to drive the MOSFET  $S_1$  and  $S_2$ , and the system frequency is determined by  $S_a$ .

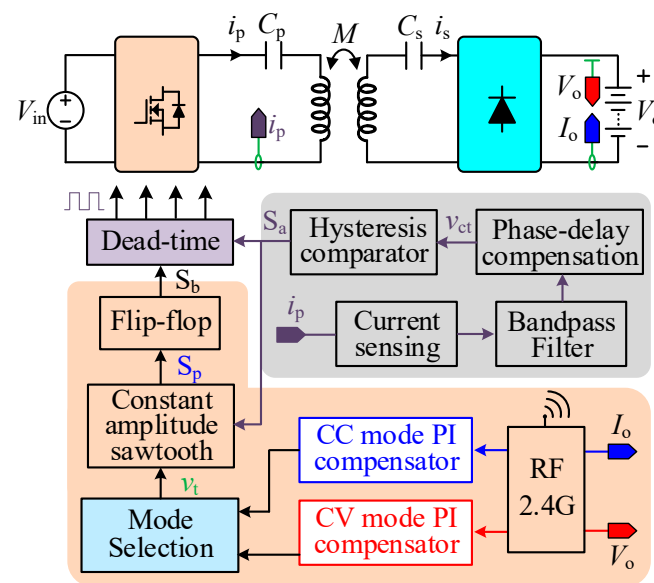


**Figure 8.** The diagram of IPT charging system with SO-PS control.

Meanwhile, in the battery charging control loop, the smaller PI output between the CC mode and the CV mode is selected to determine which charging mode should remain. To be more specific, if the PI output of the CC loop is smaller than that of the CV loop, then CC mode will be selected. The PI value is determined by the integral of past difference between the reference value and the measured value. It is assumed that, initially, both the CC loop and CV loop have the minimum PI output and the reference values are higher than the initial values; this would mean that the differences are positive, which would result in an increment in the respective PI output. The system will start with the CC mode because the current will first reach its reference value and the difference between the reference current and measured current is zero; then, its PI output stops increasing. However, the voltage is far from its reference value at this stage, so the PI of the CV loop is saturated and remains at

the maximum value, making it larger than that of the CC mode. Based on the principle that a smaller PI output will be selected, the mode selection picks up the CC mode accordingly. During the transition from a CC mode to a CV mode, as the system still operates at a CC mode and the equivalent load resistance keeps growing, the actual voltage exceeds the reference voltage, leading to a negative difference for the voltage control loop. Then, the PI output of the CV loop will become desaturated and begin to decrease until it becomes lower than that of the CC loop. From then on, the system switches to CV mode, and will not return to CC mode. Figure 9 illustrates the flow chart of the hybrid control strategy.

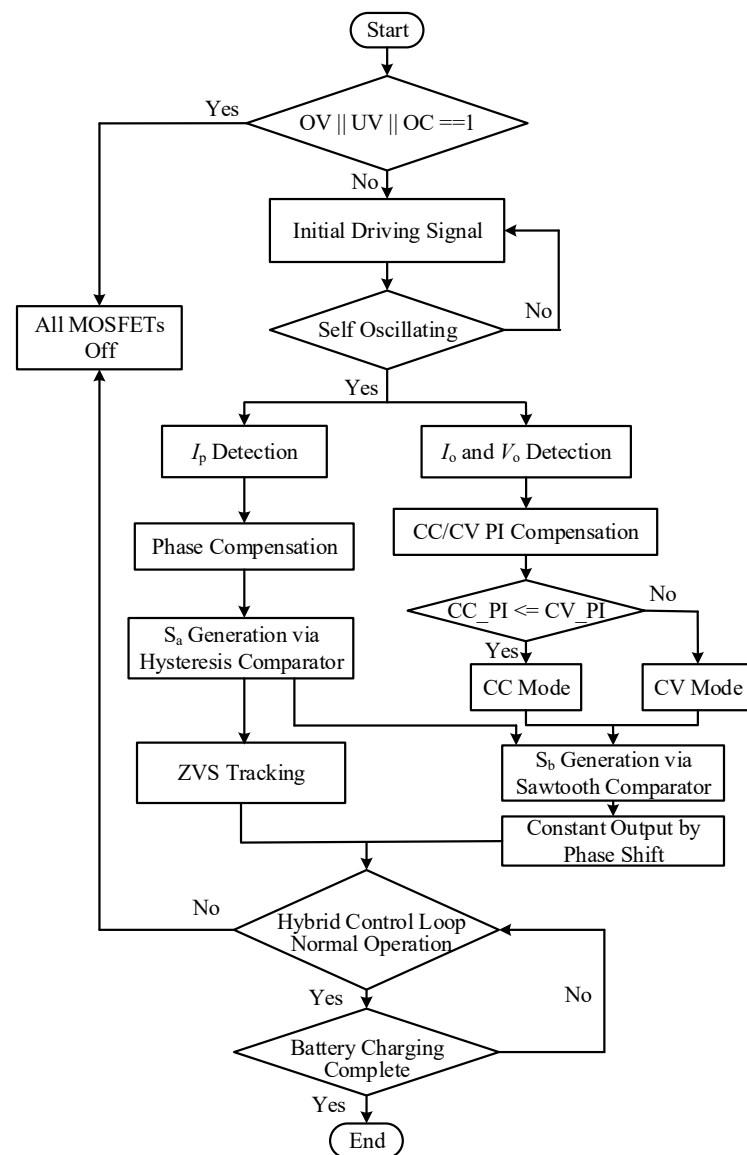


**Figure 9.** Flow chart of SO-PS control strategy.

To show more details of the control circuit, Figure 10 illustrates the inner structure of important control units. It can be observed that the self-oscillation is completed by an analog circuit, and the phase shift is realized by a microprocessor. Each unit is analyzed as follows. The primary current is sampled by the current sensing circuit and the sinusoidal signal  $v_{ip}$  is first filtered by a bandpass filter to get rid of higher-order harmonics. Afterwards, to implement accurate control on the system, phase delay should be considered; therefore, a phase-delay compensation circuit is added, whose output is  $v_{ct}$ , as illustrated in Figure 11.

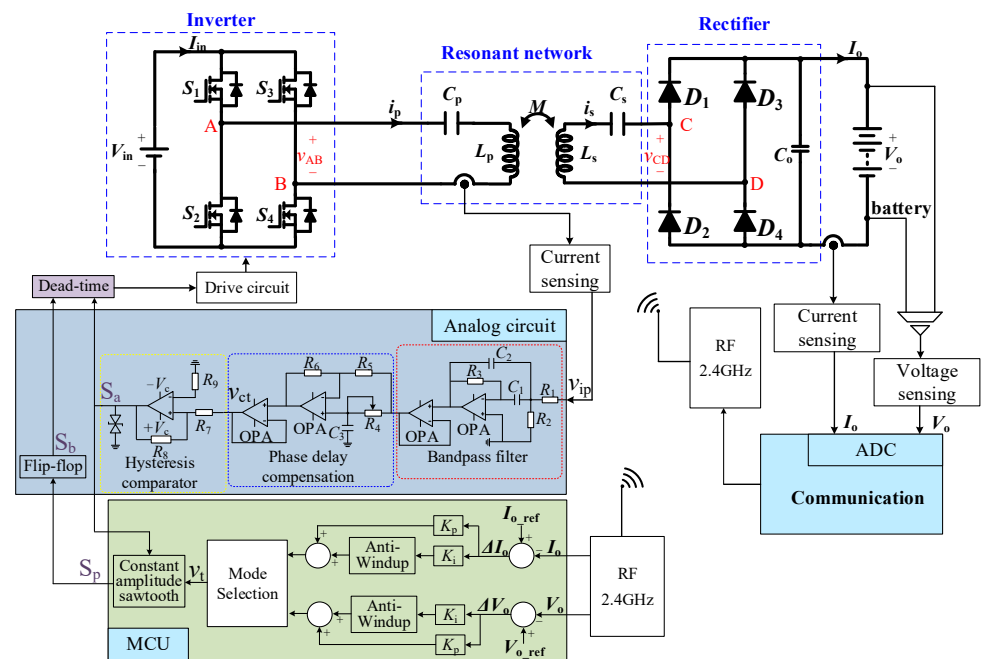


Figure 10. Proposed control circuit for IPT system.

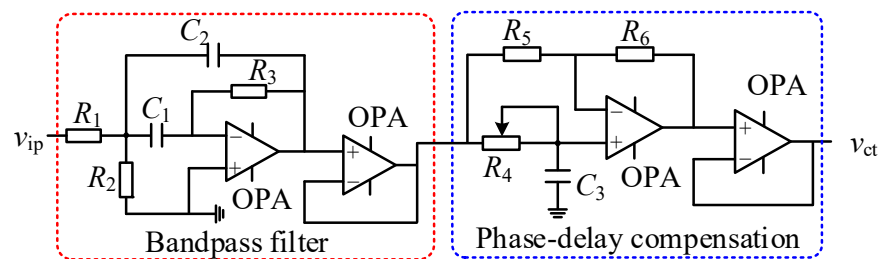


Figure 11. Schematic diagrams of Bandpass filter and phase-delay compensation circuit.

In contrast with the ZVS realization method reported in [28,29], the drive signal of the lagging leg is directly generated by a hysteresis comparator, and the corresponding hysteresis band width is determined by the minimal commutation current  $I_{ZVS,ref}$ , which can be calculated by

$$I_{ZVS,ref} = \frac{4C_{oss}V_{inmax}}{t_d} \tag{19}$$

The operation principle waveforms and hysteresis comparator circuit are shown in Figure 12.  $V_{ct}$  is the output voltage signal of the phase-delay compensation circuit and input voltage signal of the hysteresis comparator, which satisfies  $v_{ct} = \tau i_p$ , where  $\tau$  is a coefficient.

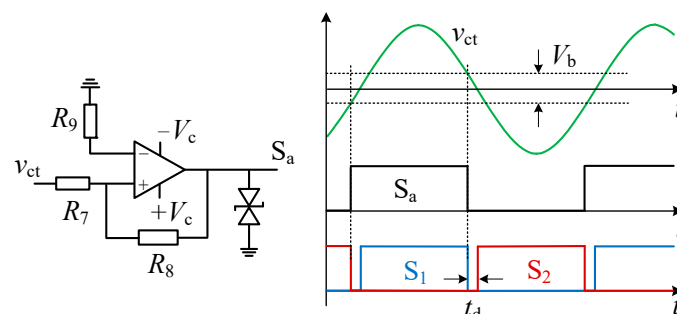


Figure 12. Schematic diagrams of hysteresis comparator circuit and waveform.

From Figure 12, the hysteresis band width  $V_b$  can be calculated by

$$V_b = \frac{V_{ct}R_7}{R_8} = \frac{4\tau C_{oss}V_{inmax}}{t_d} \quad (20)$$

In this specific design,  $S_a$  would be used to switch on  $S_1$  at the crossing point of  $V_b$  and  $v_{ct}$ . As  $v_{ct}$  represents  $i_p$ , and  $V_b$  is proportional to  $I_{zvs,ref}$ , the crossing point indicates that the primary-side current  $i_p$  at this time equals  $I_{zvs,ref}$ . If  $S_1$  can be switched on at this point, the commutation current at the rising edge of  $v_p$  equals  $I_{zvs,ref}$ , and can be used to realize ZVS. The same is true for  $S_2$ : at the falling edge of  $S_a$ , the primary-side current  $i_p$  equals  $I_{zvs,ref}$  again, and can guarantee the ZVS of  $S_2$ .

In order to achieve CC-CV charging, the falling edge of  $v_p$  should be determined as well. In other words, the gate signal of  $S_3(S_4)$  and  $S_a$  must be synchronized with a controllable phase delay  $\theta$ . The practical implementation waveforms are given in Figure 13. The main idea of the synchronization method is to generate a constant-amplitude sawtooth  $S_w$  according to the variations in switching frequency in a microprocessor. Hence, the PI output of the CC/CV charging loop  $v_t$  can be compared with  $S_w$ , resulting in a pulse  $S_p$ . The pulse  $S_p$  is used to set and reset a flip-flop whose output is defined as  $S_b$ .  $S_b$  would be used to control the turning on and off for  $S_3$  and  $S_4$ . Consequently, both  $S_a$  and  $S_b$  input the dead-time module to define the gate signals, which can avoid any probability of the shoot-through of the MOSFETs.

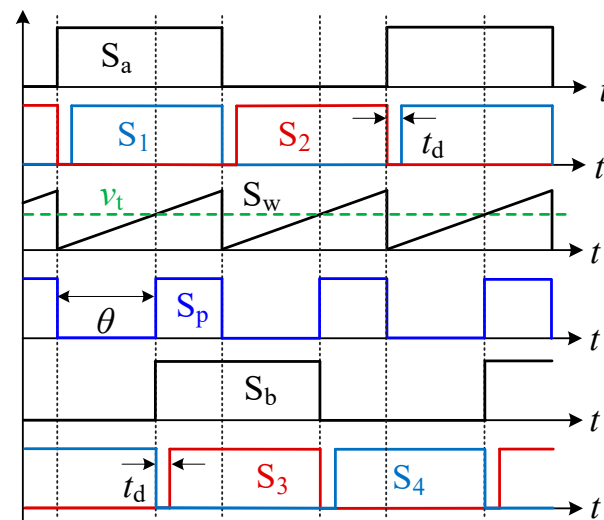
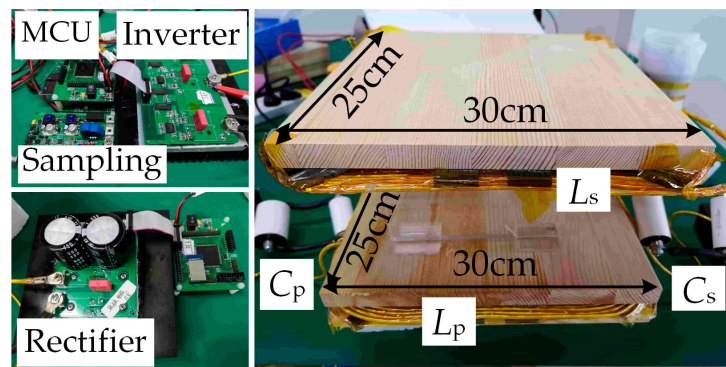


Figure 13. Practical implementation waveforms of synchronization.

Based on the implementation given above, the IPT system with a hybrid control strategy can achieve ZVS and CC/CV output simultaneously.

#### 4. Experimental Verifications

As shown in Figure 14, a 1.6-kW IPT battery charging system was designed and built to validate the proposed hybrid control strategy. Two rectangular coils, separated by a 10–15 cm air gap, were used to couple the primary side with the secondary side. Both coupled coils are formed of a 600-strand Litz wire, and the coils are 30 cm × 25 cm in size. The thickness of the coils is about 10 mm, including the ferrite bars. The primary coil has 18 turns, and the secondary coil has 24 turns.



**Figure 14.** Experimental prototype of the proposed IPT charging system.

The electrical parameters of the prototype system are listed in Table 2. The primary coil current  $i_p$  is measured using the current transducer LA-25P with galvanic separation. A sampling circuit is employed on the primary side. A DC source (Chroma 62150H) is employed, and an electric load (Chroma 63206E) serves as the adjustable load resistor.

**Table 2.** Electrical parameters of the prototype.

Parameters	Symbol	Value
Primary coil inductor	$L_p$	239.7 $\mu$ H
Primary compensation capacitor	$C_p$	18.7 nF
Secondary coil inductor	$L_s$	332.1 $\mu$ H
Secondary compensation capacitor	$C_s$	13.5 nF
Coupling coefficient	$k$	0.2–0.3
Power MOSFETs	$S_1$ – $S_4$	FCH76N60NF
Rectifier diodes	$D_1$ – $D_4$	DSEI120-06A

Before the battery charger operation, the amplitude of the primary coil current is zero, and no signal can be employed to start the oscillations. Hence, a starting process should be applied to provide initial driving signals. Here,  $S_2$  and  $S_3$  switches are turned on:  $v_p = -V_{in}$ . Then,  $S_1$  and  $S_4$  are turned on, while  $S_2$  and  $S_3$  are turned off. The inverter applies a step voltage to the resonant network with an amplitude of the input voltage. The state of the switches is changed when the rising edge of  $S_a$  is detected, meaning that the inverter is undergoing a self-oscillation operation.

#### 4.1. Operation Waveforms

According to (25) and the datasheet of the adopted MOSFETs, the minimal commutation current  $I_{zvs,ref}$  can be determined as 3 A when considering some margins. The steady-state operation waveforms of the IPT charging system at different  $k$  conditions are shown in Figure 15. The charging current is 4 A in CC mode and the charging voltage is 400 V in CV mode, regardless of  $k$ . The critical coupling coefficient can be calculated as  $k_c = 0.25$ . As seen from Figure 15a,c, when  $k = 0.2$ , this means that bifurcation did not occur and the communication current  $I_{zvs}$  is approximately 3.10 A and 3.11 A. In Figure 15b,d,  $k = 0.3 > k_c$ , which means that bifurcation occurred, and the measured switching frequency is 94.6 kHz, i.e.,  $\gamma = 1.24$ . In addition, the communication current  $I_{zvs}$  is about 2.95 A and 2.87 A.

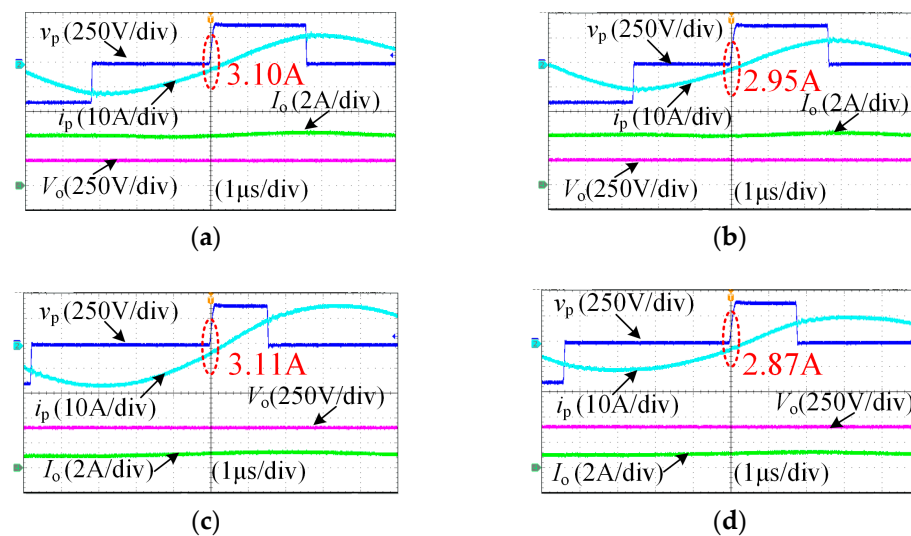


**Figure 15.** Experimental waveforms at  $V_{in} = 400$  V condition. (a) CC mode,  $k = 0.2$ , (b) CC mode,  $k = 0.3$ , (c) CV mode,  $k = 0.2$ , and (d) CV mode,  $k = 0.3$ .

To verify the robust performance of the proposed hybrid control method, experimental results were measured with a  $V_{in}$  that changed from 380 V to 420 V when  $k = 0.3$ . As shown in Figure 16a,  $I_o$  can be maintained at a steady state of 4 A with a slight overshoot when the input voltage changes in CC mode. The communication currents  $I_{ZVS}$  are 2.9 A and 3.1 A. Similarly, the output voltage  $V_o$  is almost unchanged in CV mode, as shown in Figure 16b. The communication currents  $I_{ZVS}$  are 2.85 A and 3.07 A, respectively. The response time of the control system is around 40 ms.

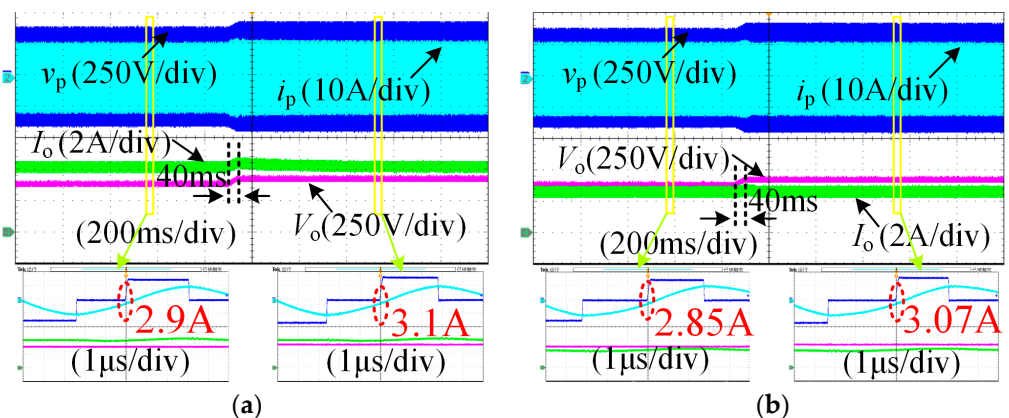


**Figure 16.** Experimental waveforms at  $k = 0.3$  conditions when  $V_{in}$  changes from 380 V to 420 V. (a) CC mode, (b) CV mode.

The experimental results were measured when the load suddenly changed, as shown in Figure 17. It should be emphasized that the equivalent resistance of the battery pack cannot abruptly change in practical applications. Here, the sudden change in the equivalent resistance  $R_L$  was only used to test the dynamic performance of the proposed control strategy. Figure 17 shows that the proposed IPT system can maintain a constant output current in CC mode and a constant output voltage in CV mode when the load changes. From the enlarged view of Figure 17a,b, it is clear that ZVS is achieved. The response time of  $R_L$  changed in CC mode in the control system is around 320 ms, and the response time of  $R_L$  changed in CV mode in the control system is around 20 ms.

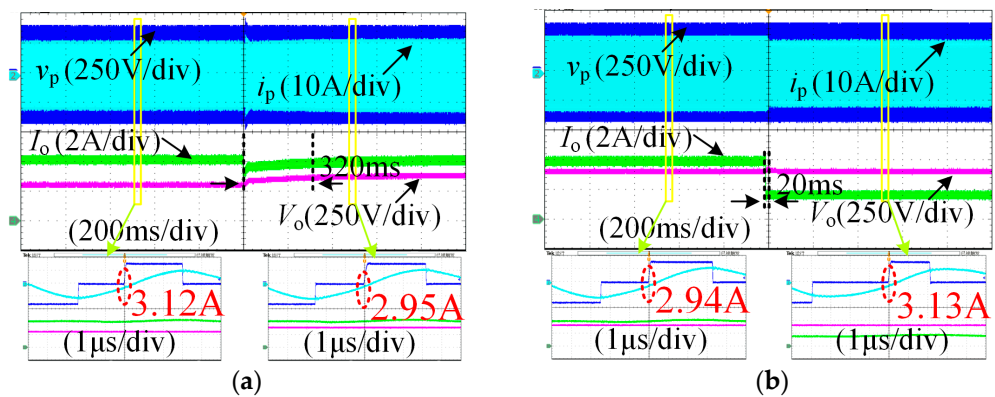


**Figure 17.** Experimental waveforms at  $k = 0.3$ ,  $V_{in} = 400$  V condition. (a) In CC mode when the  $R_L$  changes from  $75 \Omega$  to  $95 \Omega$ , (b) in CV mode when the  $R_L$  changes from  $105 \Omega$  to  $265 \Omega$ .

The CC mode will be switched to CV mode when the battery voltage is increased to 400 V. Figure 18 shows that the CC mode can be smoothly changed to CV mode by comparing the corresponding PI values. Clearly, the ZVS is obtained with  $I_{ZVS} = 3.01$  A and  $I_{ZVS} = 2.88$  A. The response time of CC mode changing to CV mode in the control system is around 160 ms.

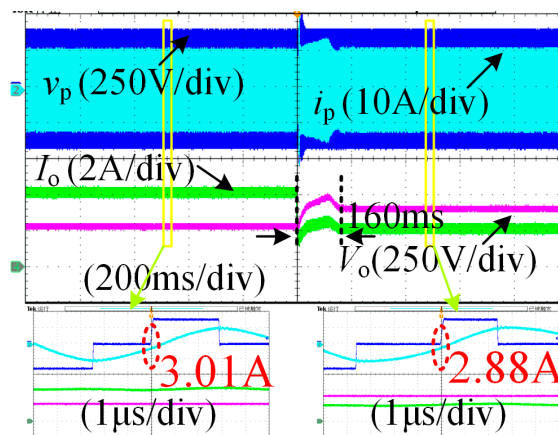


**Figure 18.** Experimental waveforms from CC mode to CV mode.

To testify the control accuracy of ZVS, the communication current errors  $\Delta I_{ZVS}$  ( $\Delta I_{ZVS} = I_{ZVS} - I_{ZVSref}$ ) were measured under various conditions, maintaining CC/CV battery charging, as shown in Figure 19. The maximum current error is about 0.2 A in comparison with the preset value.

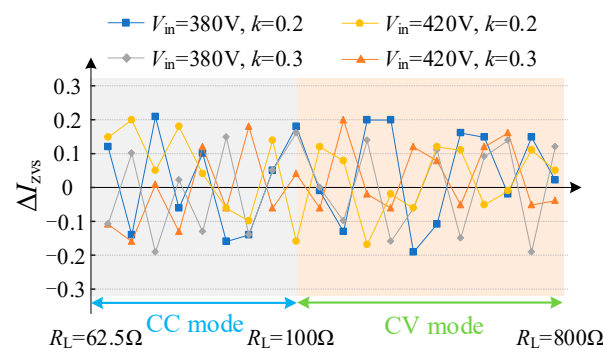


**Figure 19.** Steady-state communication currents errors of  $I_{ZVS}$ .

The measured normalized switching angle frequency  $\gamma$  of the proposed hybrid control and VF control for different coupling coefficient  $k$  and input voltage  $V_{in}$  are plotted in Figure 20. For VF control,  $\gamma$  decreases gradually in CC mode while it remains approximately constant in CV mode, in accordance with the theoretical analysis in Section 2. For the proposed hybrid control,  $\gamma$  decreases over the whole charging process and moves towards  $\gamma = 1$ . It is easy to see that the switching frequency of the proposed hybrid control is much closer to the natural resonant frequency than that of VF control, which reduces the reactive power loss. The triangles and diamonds are sampling points.

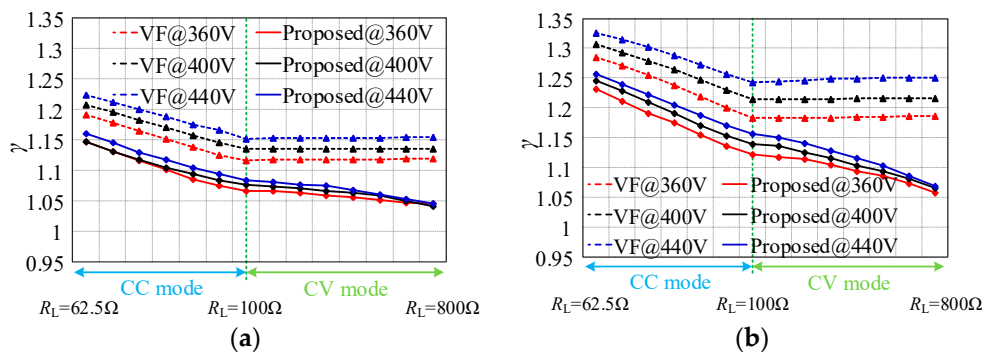


Figure 20. The measured switching frequency of proposed hybrid control and VF control. (a)  $k = 0.2$ , (b)  $k = 0.3$ .

#### 4.2. System Efficiency

The measured system efficiency of the proposed hybrid control and the conventional VF control are shown in Figure 21. The experimental results show that the maximum efficiency of the proposed control is 96.7% when  $V_{in} = 360$  V,  $k = 0.3$ , and  $P_o = 1$ . reaches 6 kW in CC mode. Compared with conventional VF control, the maximum efficiency improvement in the proposed hybrid control is approximately 2.9% in CC mode, while it is 4.1% in CV mode. The results show that the adoption of phase shift control can provide a more flexible way to achieve the constant output control target. The triangles and diamonds are sampling points.

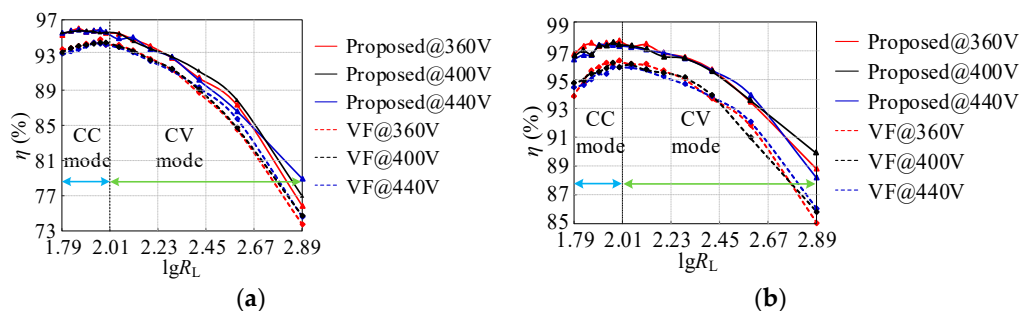


Figure 21. The measured overall efficiency of the IPT charging system. (a)  $k = 0.2$ , (b)  $k = 0.3$ .

### 5. Discussion

The hybrid control strategy has been widely used in the SS-compensated IPT charging system since, compared with a single-variable control strategy such as VF control, an additional control variable can provide more degrees of freedom, which contributes to achieving the control target. For example, in this work, with the help of phase shift control, the operating frequency is closer to the natural resonant frequency, reducing the reactive power. Some of the existing literature applied their hybrid control model to the full-bridge inverter to tune the operating frequency, whereas some used additional components, such as a variable inductor or capacitor, to change the parameters of the compensation network with a constant operating frequency. The control strategies mentioned above

adjust the phase angle between the primary inverter voltage and current. The advantage of the frequency-tuning method is the elimination of power loss produced by additional components, and the advantage of the variable inductor or capacitor methods is to avoid potential instability caused by bifurcation issues. Table 3 provides a comparison to other control strategies.

**Table 3.** Comparison with other relevant control techniques.

	Control Strategy	Input Voltage	Maximum Power	Battery Voltage	System Efficiency	Output Type
[28]	PWM-PLL	30–60 V	60 W	24 V	87.8%	CV
[29]	SOS PS-PWM	50 V	220 W	50 V	88%	CV
[31]	VF-PS	80 V	288 W	32–72 V	94.9%	CC-CV
[33]	VI-PS	100 V	170 W	72 V	92%	CV
[34]	SC-PS	30 V	10 W	26 V	87%	CC-CV
This work	SO-PS	360–440 V	1.6 kW	250–400 V	96.7%	CC-CV

For the future scope and an insight into the further developments, in this work, a hybrid control strategy is studied and implemented. However, there is not adequate research on the modelling of the control system and parameter design. In order to optimize the system parameter, reduce the response time, and increase the system efficiency, it is necessary to build up the system modelling to improve the system performance and corresponding experiments should be conducted to demonstrate the effectiveness of the modelling.

## 6. Conclusions

An SO-PS hybrid control strategy for an SS-compensated IPT system is studied and implemented in this paper to realize CC-CV battery charging and ZVS simultaneously. The hybrid control makes the switching frequency close to the resonant frequency throughout the whole charging process. The commutation current for ZVS always remains constant, regardless of the variation in the coupling coefficient and the load. Hardware implementation was carried out, and the effectiveness of the proposed control strategy was verified by an experimental prototype. The maximum efficiency is 96.7%, with  $V_{in} = 360$  V,  $k = 0.3$ , and  $P_o = 1.6$  kW.

**Author Contributions:** Conceptualization, L.H.; supervision, C.-K.L.; visualization, X.W. All authors have read and agreed to the published version of the manuscript.

**Funding:** This research was funded by Theme-based Research Scheme (T23-701/20-R).

**Institutional Review Board Statement:** Not applicable.

**Informed Consent Statement:** Not applicable.

**Data Availability Statement:** No new data were created or analyzed in this study. Data sharing is not applicable to this article.

**Conflicts of Interest:** The authors declare no conflict of interest.

## Abbreviations

The following abbreviations are used in this manuscript:

IPT	Inductive power transfer
ZVS	Zero voltage switching
CC	Constant current
CV	Constant voltage

SO	Self-oscillating
PS	Phase shift
SS	Series-series
VF	Variable frequency
EV	Electric vehicle
EMI	Electromagnetic interference
ZPA	Zero phase angle
PWM	Pulse width modulation
PDM	Pulse density modulation
PLL	Phase-locked loop
VI	Variable inductor
FHA	Fundamental harmonic approximation
$V_{in}$	DC input voltage
$S_i$	$i$ th MOSFET in the inverter
$C_p$	Primary-side capacitor
$L_p$	Transmitter coil
$L_s$	Receiver coil
$C_s$	Secondary-side capacitor
$D_i$	$i$ th diode in the rectifier
$C_o$	Output filter capacitor
$V_o$	Charging voltage
$I_o$	Charging current
$v_p$	Inverter output voltage
$i_p$	Inverter output current
$v_s$	Rectifier input voltage
$i_s$	Rectifier input current
$R_{ac}$	Equivalent load resistance
$M$	Mutual Inductance
$\omega$	Switching angular frequency of the system
$I_{zvs}$	Commutation current
$\alpha$	Inductance ratio of transmitter coil over receiver coil
$\gamma$	Normalized switching frequency
$X_{Ls}$	Impedance of receiver coil
$Q$	Load quality factor
$G_v$	Steady-state voltage gain
$\varphi$	Input impedance angle
$k$	Coupling coefficient
$d$	Air gap
$D_{out}$	Maximum coil diameter
$R_L$	Load resistance
$Q_r$	Charge on the parasitic capacitor of the MOSFET
$C_{oss}$	Capacitance of parasitic capacitor of the MOSFET
$V_{ds}$	Drain-source voltage of the parasitic capacitor of the MOSFET

## References

1. Ahn, D.; Hong, S. Wireless power transmission with self-regulated output voltage for biomedical implant. *IEEE Trans. Ind. Electron.* **2014**, *61*, 2225–2235. [[CrossRef](#)]
2. Xiao, C.; Cheng, D.; Wei, K. An LCC-C compensated wireless charging system for implantable cardiac pacemakers: Theory, experiment, and safety evaluation. *IEEE Trans. Power Electron.* **2018**, *33*, 4894–4905. [[CrossRef](#)]
3. Jang, Y.; Jovanovic, M.M. A contactless electrical energy transmission system for portable-telephone battery chargers. *IEEE Trans. Ind. Electron.* **2003**, *50*, 520–527. [[CrossRef](#)]
4. Hui, S.Y.R.; Ho, W.W.C. A new generation of universal contactless battery charging platform for portable consumer electronic equipment. *IEEE Trans. Power Electron.* **2005**, *20*, 620–627. [[CrossRef](#)]
5. Zhao, L.; Thrimawithana, D.; Madawala, U. Hybrid bidirectional wireless EV charging system tolerant to pad misalignment. *IEEE Trans. Ind. Electron.* **2017**, *64*, 7079–7086. [[CrossRef](#)]
6. Guo, Y.; Wang, L.; Zhu, Q.; Liao, C.; Li, F. Switch-on modeling and analysis of dynamic wireless charging system used for electric vehicles. *IEEE Trans. Ind. Electron.* **2016**, *63*, 6568–6579. [[CrossRef](#)]

7. Chen, C.; Zhou, H.; Deng, Q.; Hu, W.; Yu, Y.; Lu, X.; Lai, J. Modeling and decoupled control of inductive power transfer to implement constant current/voltage charging and zvs operating for electric vehicles. *IEEE Access* **2018**, *6*, 59917–59928. [[CrossRef](#)]
8. Li, Z.; Zhu, C.; Jiang, J.; Song, K.; Wei, G. A 3-kW wireless power transfer system for sightseeing car supercapacitor charge. *IEEE Trans. Power Electron.* **2017**, *32*, 3301–3316. [[CrossRef](#)]
9. Kim, J.H.; Lee, B.S.; Lee, J.H.; Lee, S.H.; Park, C.B.; Jung, S.M.; Lee, S.G.; Yi, K.P.; Baek, J. Development of 1-MW inductive power transfer system for a high-speed train. *IEEE Trans. Ind. Electron.* **2015**, *62*, 6242–6250. [[CrossRef](#)]
10. Jiang, Y.; Chen, K.; Zhao, Z.; Yuan, L.; Tan, T.; Lin, Q. Designing an M-Shape Magnetic Coupler for the Wireless Charging System in Railway Applications. *IEEE Trans. Power Electron.* **2022**, *37*, 1059–1073. [[CrossRef](#)]
11. Chan, C.C.; Jian, L.; Tu, D. Smart charging of electric vehicles—Integration of energy and information. *IET Electr. Syst. Transp.* **2014**, *4*, 89–96. [[CrossRef](#)]
12. He, L.; Zhao, S.; Wang, X.; Lee, C.-K. Artificial Neural Network-Based Parameter Identification Method for Wireless Power Transfer Systems. *Electronics* **2022**, *11*, 1415. [[CrossRef](#)]
13. Bosshard, R.; Kolar, J.W. Inductive power transfer for electric vehicle charging: Technical challenges and tradeoffs. *IEEE Power Electron. Mag.* **2016**, *3*, 22–30. [[CrossRef](#)]
14. Al-Saadi, M.; Al-Omari, A.; Al-Chlahawi, S.; Al-Gizi, A.; Crăciunescu, A. Inductive Power Transfer for Charging the Electric Vehicle Batteries. *Electroteh. Electron. Autom.* **2018**, *66*, 29–39.
15. Jiang, Y.; Wang, L.; Wang, Y.; Liu, J.; Li, X.; Ning, G. Analysis, design, and implementation of accurate ZVS angle control for EV battery charging in wireless high-power transfer. *IEEE Trans. Ind. Electron.* **2019**, *66*, 4075–4085. [[CrossRef](#)]
16. Wang, X.; He, L.; Xu, J.; Lee, C.K. Widening the Operating Range of a Wireless Charging System Using Tapped Transmitter Winding and Bifrequency Pulse Train Control. *IEEE Trans. Power Electron.* **2022**, *37*, 13874–13883. [[CrossRef](#)]
17. Deng, P.; Tang, C.; Fan, Y.; Sun, M.; Liu, Z.; Li, X. A Frequency Regulation Strategy for Dynamic Process Noise Suppression in LCC-S WPT Systems. *IEEE Trans. Power Electron.* **2022**, *37*, 13978–13988. [[CrossRef](#)]
18. Qu, X.; Han, H.; Wong, S.; Tse, C.K.; Chen, W. Hybrid IPT topologies with constant current or constant voltage output for battery charging applications. *IEEE Trans. Power Electron.* **2015**, *30*, 6329–6337. [[CrossRef](#)]
19. Mai, R.; Chen, Y.; Li, Y.; Zhang, Y.; Cao, G.; He, Z. Inductive Power Transfer for Massive Electric Bicycles Charging Based on Hybrid Topology Switching with a Single Inverter. *IEEE Trans. Power Electron.* **2017**, *32*, 5897–5906. [[CrossRef](#)]
20. Chen, Y.; Yang, B.; Li, Q.; Feng, H.; Zhou, X.; He, Z.; Mai, R. Reconfigurable Topology for IPT System Maintaining Stable Transmission Power over Large Coupling Variation. *IEEE Trans. Power Electron.* **2020**, *35*, 4915–4924. [[CrossRef](#)]
21. Qu, X.; Jing, Y.; Han, H.; Wong, S.; Tse, C.K. Higher order compensation for inductive-power-transfer converters with constant-voltage or constant-current output combating transformer parameter constraints. *IEEE Trans. Power Electron.* **2017**, *32*, 394–405. [[CrossRef](#)]
22. Vu, V.; Tran, D.; Choi, W. Implementation of the constant current and constant voltage charge of inductive power transfer systems with the double-sided LCC compensation topology for electric vehicle battery charge applications. *IEEE Trans. Power Electron.* **2018**, *33*, 7398–7410. [[CrossRef](#)]
23. Song, K.; Li, Z.; Jiang, J.; Zhu, C. Constant current/voltage charging operation for series-series and series-parallel compensated wireless power transfer systems employing primary-side controller. *IEEE Trans. Power Electron.* **2018**, *33*, 8065–8080. [[CrossRef](#)]
24. Gati, E.; Kampitsis, G.; Manias, S. Variable Frequency Controller for Inductive Power Transfer in Dynamic Conditions. *IEEE Trans. Power Electron.* **2017**, *32*, 1684–1696. [[CrossRef](#)]
25. Li, H.; Wang, K.; Fang, J.; Tang, Y. Pulse density modulated ZVS full-bridge converters for wireless power transfer systems. *IEEE Trans. Power Electron.* **2019**, *34*, 369–377. [[CrossRef](#)]
26. Xu, L.; Chen, Q.; Ren, X.; Wong, S.; Tse, C.K. Self-oscillating resonant converter with contactless power transfer and integrated current sensing transformer. *IEEE Trans. Power Electron.* **2017**, *32*, 4839–4851. [[CrossRef](#)]
27. Namadmalan, A. Self-oscillating tuning loops for series resonant inductive power transfer systems. *IEEE Trans. Power Electron.* **2016**, *31*, 7320–7327. [[CrossRef](#)]
28. Chen, Q.; Wong, S.C.; Tse, C.K.; Ruan, X. Analysis, design, and control of a transcutaneous power regulator for artificial hearts. *IEEE Trans. Biomed. Circuits Syst.* **2009**, *3*, 23–31. [[CrossRef](#)]
29. Namadmalan, A. Self-Oscillating Pulsewidth Modulation for Inductive Power Transfer Systems. *IEEE Trans. Emerg. Sel. Topics Power Electron.* **2020**, *8*, 1813–1820. [[CrossRef](#)]
30. Jiang, Y.; Wang, L.; Wang, Y.; Liu, J.; Wu, M.; Ning, G. Analysis, design, and implementation of WPT system for EV's battery charging based on optimal operation frequency range. *IEEE Trans. Power Electron.* **2019**, *34*, 6890–6905. [[CrossRef](#)]
31. Jiang, Y.; Liu, J.; Hu, X.; Wang, L.; Wang, Y.; Ning, G. An optimized frequency and phase shift control strategy for constant current charging and zero voltage switching operation in series-series compensated wireless power transmission. *IEEE Energy Convers. Congr. Expo.* **2017**, 961–966.
32. Li, Y.; Sun, W.; Zhu, X.; Hu, J. A Hybrid Modulation Control for Wireless Power Transfer Systems to Improve Efficiency Under Light-Load Conditions. *IEEE Trans. Ind. Electron.* **2022**, *69*, 6870–6880. [[CrossRef](#)]
33. Li, Y.; Liu, S.; Zhu, X.; Hu, J.; Zhang, M.; Mai, R.; He, Z. Extension of ZVS Region of Series-Series WPT Systems by an Auxiliary Variable Inductor for Improving Efficiency. *IEEE Trans. Power Electron.* **2021**, *36*, 7513–7525. [[CrossRef](#)]
34. Kavimandan, U.D.; Mahajan, S.M.; Van Neste, C.W. Analysis and Demonstration of a Dynamic ZVS Angle Control Using a Tuning Capacitor in a Wireless Power Transfer System. *IEEE Trans. Emerg. Sel. Topics Power Electron.* **2021**, *9*, 1876–1890. [[CrossRef](#)]

35. Ganapathie, M.; Alavandar, S.; Kasinathan, P.; Sowmmiya, U.; Ramachandaramurthy, V.K.; Pachaivannan, N. Evaluation of hybrid controllers for space vector modulation-inverter driven permanent magnet synchronous motor-pump assembly. *ISA Trans.* **2022**, *128*, 635–649. [[CrossRef](#)]
36. Zhang, W.; Wong, S.C.; Tse, C.K. Chen. Design for Efficiency Optimization and Voltage Controllability of Series–Series Compensated Inductive Power Transfer Systems. *IEEE Trans. Power Electron.* **2014**, *29*, 191–200. [[CrossRef](#)]
37. Li, S.; Li, W.; Deng, J.; Nguyen, T.D.; Mi, C.C. A Double-Sided LCC Compensation Network and Its Tuning Method for Wireless Power Transfer. *IEEE Trans. Veh. Technol.* **2015**, *64*, 2261–2273. [[CrossRef](#)]
38. Wang, C.-S.; Covic, G.A.; Stielau, O.H. Power transfer capability and bifurcation phenomena of loosely coupled inductive power transfer systems. *IEEE Trans. Ind. Electron.* **2004**, *51*, 148–157. [[CrossRef](#)]
39. Youssef, M.Z.; Pinheiro, H.; Jain, P.K. Self-sustained phase-shift modulated resonant converters: Modeling, design, and performance. *IEEE Trans. Power Electron.* **2006**, *21*, 401–414. [[CrossRef](#)]
40. Youssef, M.Z.; Jain, P.K. Series–parallel resonant converter in self-sustained oscillation mode with the high-frequency transformer-leakage-inductance effect: Analysis, modeling, and design. *IEEE Trans. Ind. Electron.* **2007**, *54*, 1329–1341. [[CrossRef](#)]

**Disclaimer/Publisher’s Note:** The statements, opinions and data contained in all publications are solely those of the individual author(s) and contributor(s) and not of MDPI and/or the editor(s). MDPI and/or the editor(s) disclaim responsibility for any injury to people or property resulting from any ideas, methods, instructions or products referred to in the content.